Preparation of carbon-sensitized and Fe–Er codoped TiO$_2$ with response surface methodology for bisphenol A photocatalytic degradation under visible-light irradiation

Dianxun Hou [a], Ronn Goei [a,b], Xiaoping Wang [a], Penghua Wang [a,b], Teik-Thye Lim [a,b,*]

[a] School of Civil and Environmental Engineering, Nanyang Technological University, 50 Nanyang Avenue, Singapore 639798, Republic of Singapore
[b] Singapore Membrane Technology Centre, Nanyang Technological University, 50 Nanyang Avenue, Singapore 639798, Republic of Singapore

ARTICLE INFO

ABSTRACT

The carbon-sensitized and Fe–Er codoped TiO$_2$ (Fe/Er–TiO$_2$) was synthesized by a facile solvothermal method using titanium isopropoxide both as titanium precursor and carbon source, as well as ferric nitrate and erbium nitrate as dopants source. The response surface methodology (RSM) with central composite design (CCD) model was used to obtain the optimum synthesis conditions for this novel Fe/Er–TiO$_2$. The RSM was also applied to study the main and interactive effects of the parameters (Er concentration [Er], Fe concentration [Fe] and calcination temperature [CT]) investigated. The experimental results indicated an improved photocatalytic activity of Fe/Er–TiO$_2$ for bisphenol A (BPA) degradation compared to the pristine TiO$_2$, Er–TiO$_2$, Fe–TiO$_2$ and Degussa P25 (P25) under visible light irradiation. In addition, the RSM model obtained (R^2 = 0.929) showed a satisfactory correlation between the experimental results and predicted values of BPA removal efficiency. The identified optimum condition for preparing Fe/Er–TiO$_2$ was 1.5 mol%, 1.25 mol% and 450 °C for [Er], [Fe] and [CT], respectively. Moreover, the photocatalytic activity of the optimized Fe/Er–TiO$_2$ was preserved effectively even after ten cycles of use. The possible photocatalytic mechanisms induced by the Fe/Er–TiO$_2$ under visible light irradiation are proposed. The enhanced photocatalytic activity of Fe/Er–TiO$_2$ can be attributed to the synergistic effects of photosensitizing (C—O band), narrowed band gap and enhanced e$^-$/h$^+$ separation (Ti–O–Fe linkage), and upconversion luminescence property (Ti–O–Er linkage).

© 2012 Elsevier B.V. All rights reserved.

1. Introduction

Bisphenol A (BPA) is an endocrine disrupter which has been widely used as a precursor in synthesis of epoxy resins and polycarbonate plastics [1]. It cannot be removed in the conventional wastewater treatment processes due to its bio-refractory nature. Thus, it is frequently found in urban wastewaters, treated effluents and surface waters [2].

TiO$_2$ has been widely investigated for photocatalytic degradation of organic pollutants because of its strong photocatalytic ability, high stability, non-toxicity and low cost [3,4]. However, the solar light utilization efficiency of the virgin TiO$_2$ is less than 5% (i.e. UV component) [5], which limits its commercial application for water and wastewater treatment. Hence, considerate efforts have been devoted to modifying TiO$_2$ in order to extend its absorption band-edge into the visible light region. Several approaches

including doping of non-metals (C, N, F, S) [6–11], metals (V, Cr, and Fe) [12–14] and rear earth upconversion luminescence agents [15–20] into TiO$_2$ have been developed to achieve this goal. C, Fe and Er are among most studied elements in the three dopant groups, respectively.

Most recently, it has been reported that simultaneously doping of two or three dopants into TiO$_2$ could significantly enhance its visible-light responses as compared to the enhancement through single element doping [21,22]. For example, Wang et al. [22] synthesized Fe–C codoped TiO$_2$ via a facile solvothermal method for photocatalytic degradation of BPA and clofibric acid (CA). Wang et al. [21] prepared the carbon-sensitized and nitrogen-doped TiO$_2$ by a facile sol–gel method using titanium butoxide for the degradation of sulfanilamide (SNM). Zhou et al. [23] synthesized Er^{3+} doped Bi$_2$MoO$_6$ for the degradation of organic dyes.

Based on the above studies, we hypothesize that the carbon sensitized and Fe–Er codoped TiO$_2$ (Fe/Er–TiO$_2$) combining the synergistic effects of photosensitizing [24,25], narrowed band gap and enhanced e$^-$/h$^+$ separation [26–28], and upconversion luminescence property [29] introduced by C, Fe and Er, respectively, may have a superbly enhanced photocatalytic activity. To our best

* Corresponding author at: School of Civil and Environmental Engineering, Nanyang Technological University, 50 Nanyang Avenue, Singapore 639798, Republic of Singapore. Tel.: +65 6790 6933; fax: +65 6791 0676.
E-mail address: cttlim@ntu.edu.sg (T.-T. Lim).

Table 1
Independent variables and their levels for the CCD experiment.

Variables	Ranges and levels				
	−2	−1	0	1	2
Er concentration (mol %) [Er]	0	0.5	1	1.5	2
Fe concentration (mol %) [Fe]	0	1.25	2.5	3.75	5
Calcination temperature (°C) [CT]	400	450	500	550	600

knowledge, no study on this novel modified TiO_2 for visible-light photocatalysis has been reported.

The response surface methodology (RSM) has been proved to be a powerful statistical technique for obtaining optimum conditions for advanced oxidation processes and evaluating the interactions of mutually influencing parameters with a limited number of experiments [30–34]. However, as far as we know, most of these studies were focused on photocatalytic degradation (PCD) experiments [30,34]. Comparatively, much fewer scientific works have been published dealing with the application of RSM in the preparation of the photocatalyst [35,36].

In this study, RSM was introduced in the synthesis of $Fe/Er–TiO_2$ in order to identify the optimized conditions (Fe concentration [Fe], Er concentration [Er] and calcination temperature [CT]) important for photocatalyst preparation via a facile solvothermal method. The synergistic effects of Fe and Er codoping on crystallite size, surface area, light absorption behavior and photocatalytic performance of the resulting $Fe/Er–TiO_2$ were evaluated. BPA was chosen as the target pollutant to be degraded. To evaluate the action spectrum of the synthesized photocatalysts, different visible LED lights that emit white, blue, green, yellow and red lights, as well as simulated solar light were used as the excitation light sources.

2. Methodology

2.1. Photocatalyst preparation

All chemicals were used as received without further purification. Deionized (DI, Millipore) water with resistivity of 18.2 MΩ cm was used throughout the study unless otherwise stated. The $Fe/Er–TiO_2$ photocatalysts were synthesized by the solvothermal method. Typically, 10 mL titanium isopropoxide (TTIP, ≥98%, Sigma–Aldrich) was dissolved in 85 mL of isopropanol (IP, ≥99%, Merck). The molar ratios of Er and Fe to Ti vary (Tables 1 and 2). A mixture solution of 3 mL H_2O, 3 mL IP and 1 mL HNO_3 (70%, Labscan) with stoichiometric amounts of $Er(NO_3)_3·6H_2O$ (99.9%, Sigma–Aldrich) and $Fe(NO_3)_3·9H_2O$ (99.9%, Merck) were added into the TTIP solution. The mixture was vigorously agitated for 1 h at room temperature and then transferred into a 125 mL Telfon-lined autoclave. The autoclave was heated and maintained at 120 °C for 4 h. The product was separated by centrifugation, thoroughly washed with DI water and then dried at 80 °C overnight. Finally the samples were calcined at various temperatures (Tables 1 and 2) for 4 h in a muffle furnace under air atmosphere with a heating rate of 5 °C min⁻¹ followed by grinding to obtain the $Fe/Er–TiO_2$ powder. The as-prepared photocatalysts are herein denoted as xFe/yEr–Ti([CT]), where x and y refer to the molar ratio (%) of Fe/Ti and Er/Ti, respectively. For comparison, the pristine TiO_2, $Er–TiO_2$ and $Fe–TiO_2$ were also prepared through the similar procedure.

A central composite design (CCD) was employed for the synthesis of $Fe/Er–TiO_2$. The RSM was used to evaluate the combined effects of three independent variables: [Er], [Fe] and [CT], designated as X_1, X_2 and X_3, respectively, on the photocatalytic performance of the resulting photocatalysts. The ranges of variables and experimental conditions determined by CCD are presented in Table 1. The experiments consisted of six axial, eight factorial and

six center points. Considering the general function expressing the interaction between the independent and dependent variables, a second-order model was employed:

$$Y = b_0 + \sum b_i X_i + \sum b_{ii} X_i^2 + \sum b_{ij} X_i X_j + \varepsilon \tag{1}$$

where Y is the response, b_0 is the constant, b_i is the linear effect of the factor X_i (i = 1, 2 and 3), b_{ii} is the quadratic effect of the factor X_i, b_{ij} is the linear interaction effect between the input factors X_i and X_j (i = 1, 2 and 3; j = 1, 2 and 3), and ε is the residual term. Design-Expert V8.05 was used for regression analysis of the experimental data. Analysis of variance (ANOVA) was also utilized to test the significance of each term in the equation and the goodness of fit of the obtained regression model. MATLAB R2011b was used to construct the response surface and contour plots.

2.2. Photocatalyst characterization

X-ray diffraction (XRD) spectra were obtained using a Bruker D8 ADVANCE X-ray Diffractometer with Cu K radiation (λ = 1.5418 Å) in a 2θ range of 5–80°. The crystallite size was obtained from MDI Jade 5.0 software. The surface chemical bonding states of the photocatalysts were analyzed by performing X-ray photoelectron spectroscopy (XPS) on a Kratos Axis Ultra spectrometer using a monochromatized Al K (1486.71 eV) X-ray source. All the spectra were calibrated against the adventitious carbon at 284.8 eV. The particle morphology and surface elemental content were examined using JEOL JSM7600 scanning electron microscope (SEM) equipped with energy dispersive X-ray spectroscopy (EDX, Rigaku Corporation). Porosimetric studies were carried out using a Quantachrome Autosorb-1 instrument at 77 K. The specific surface area was calculated using the Brunauer–Emmett–Teller (BET) equation, while the pore volume and pore diameter were obtained from the desorption branch of nitrogen adsorption/desorption isotherm using the Barrett–Joyner–Halenda (BJH) method. The UV–vis diffuse reflectance spectra (DRS) were obtained using a PerkinElmer Lambda 35 UV-vis spectrophotometer equipped with an integrating sphere assembly with $BaSO_4$ as the reflectance standard. Thermogravimetric (TG) analysis was performed using TG analyzer (Perkin Elmer) in a range of 30–900 °C with a heating rate of 5 °C min⁻¹ in an air flow. Gaseous species evolved from the sample were simultaneously analyzed with a Fourier transform infrared spectrophotometer (FT-IR, Perkin Elmer 2000). Photoluminescence (PL) emission spectra of the samples were recorded using Fluorolog-3 spectrofluorometer equipped with a Nd:YAG laser system with excitation wavelength at 320 nm (Horiba Scientific).

2.3. LED photoreactor setup

The schematic diagram of the LED photoreactor, comprising a 250 mL borosilicate glass reactor with 70 mm diameter and 95 mm height is depicted in Fig. 1. The reactor was wrapped with a 2-m LED flexible strip (SMD 5050, 15 W) with a beam angle of 120°. Five different LED strips were used in this study, emitting blue light (LED-B, λ = 465 nm), green light (LED-G, λ = 523 nm), yellow light (LED-Y, λ = 589 nm), red light (LED-R, λ = 660 nm) and white LED (LED-W) that clearly showed blue light emission (λ = 450 nm) and more broadband Stokes-shift light ($\lambda \approx$ 500–600 nm). A cooling jacket was wrapped around the photoreactor to maintain its temperature at 30 ± 5 °C throughout the experiments. A mirror cover was used to minimize water evaporation and cut off light from the ambient environment. For comparison, a solar simulator (Newport) equipped with a 150 W Xenon arc lamp, in particular the solar visible light (430–630 nm, denoted as SV) was also used as an alternative light source. The simulated solar irradiation possessed the

Table 2
CCD matrix for three variables together with physicochemical properties, the observed BPA degradation (%) and predicted values.

Run	Coded variables			Crystallite size[a] (nm)	S_{BET} [b] (m^2 g^{-1})	d_p [c] (nm)	V_p [c] (cm^3 g^{-1})	BPA degradation (%)		C_0 [d] (mg L^{-1})	k_{app} [e] (min^{-1}), 10^{-3}	r_0 [f] (mg L^{-1} min^{-1}), 10^{-3}
	[Er]	[Fe]	[CT]					Experimental	Predicted			
1	0	0	0					86.9	86.3	5.53		43.5
2	0	0	0					86.8	86.3	5.49		43.2
3	0	0	0					87.5	86.3	5.50		43.2
4	0	0	0	6.7	129.44	5.62	0.30	87.3	86.3	5.49	7.9(0.988[g])	43.2
5	0	0	0					86.9	86.3	5.58		43.9
6	0	0	0					87.0	86.3	5.54		43.5
7	1	1	1	6.4	112.90	6.56	0.34	43.8	50.0	4.62	3.0(0.947)	14.0
8	1	1	−1	6.5	163.40	4.90	0.39	69.1	72.9	4.33	4.9(0.997)	21.0
9	1	−1	1	7.1	117.20	6.56	0.34	97.0	97.4	5.17	14.1(0.964)	73.0
10	1	−1	−1	8.1	165.20	5.62	0.37	>99.0[h]	98.2	5.45	21.8(0.985)	118.7
11	−1	1	1	10.5	103.40	6.55	0.32	39.5	46.0	5.88	2.4(0.962)	14.2
12	−1	1	−1	6.1	107.90	5.63	0.25	81.2	85.4	5.82	5.9(0.940)	34.1
13	−1	−1	1	11.4	83.94	7.75	0.28	77.3	78.2	4.10	6.7(0.999)	27.5
14	−1	−1	−1	7.1	136.40	5.62	0.32	97.0	95.5	5.58	16.0(0.932)	89.5
15	−2	0	0	11.3	89.60	6.56	0.29	78.3	75.6	6.20	6.5(0.961)	40.6
16	0	−2	0	7.8	125.70	6.55	0.34	97.4	100.0	5.43	15.4(0.989)	83.8
17	0	0	−2	5.7	178.20	4.90	0.35	94.8	94.8	5.08	13.9(0.992)	70.7
18	2	0	0	6.2	122.90	5.62	0.33	84.2	82.3	5.70	7.3(0.956)	41.7
19	0	2	0	9.8	149.90	5.61	0.35	51.1	43.1	5.40	2.0(0.939)	10.5
20	0	0	2	11.1	83.42	9.57	0.27	59.2	54.6	4.65	3.5(0.976)	16.5

[a] Derived using Scherrer equation from XRD spectra.
[b] Specific surface area, calculated using the BET equation.
[c] Obtained from the desorption branch of nitrogen isotherm by the BJH method.
[d] Initial BPA concentration after adsorption/desorption equilibrium in dark.
[e] Apparent degradation rate constant.
[f] Initial degradation rate.
[g] R^2, correlation of determination.
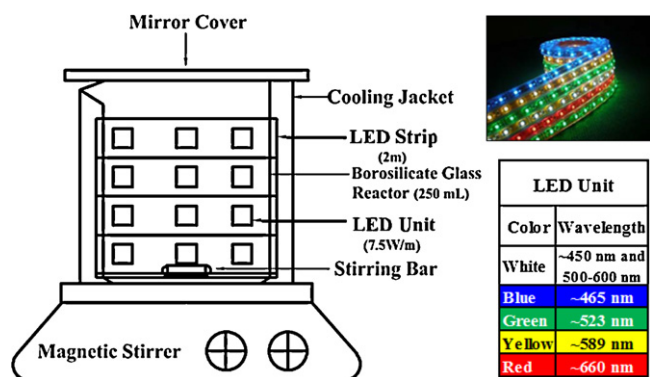[h] BPA concentration is below the limit of quantification of HPLC (0.1 mg L^{-1}).

Fig. 1. Schematic diagram of photoreactor used for photodegradation of BPA with LED strips as excitation light source.

full-spectrum light intensity of ca. 1000 W m^{-2} (one sun power) as measured by a digital power meter SP 1065 (Janco Impex) on the surface of the solution, and its UV intensity was ca. 25 W m^{-2} as measured by Accumax XRP-3000 radiometer.

2.4. Photocatalytic degradation of BPA

The PCD experiments of BPA by Fe/Er–TiO$_2$ were carried out using the above-mentioned photoreactor. In a typical PCD experiment, prior to the commencement, a 200 mL suspension containing 200 mg photocatalysts (dosage = 1 g L^{-1}) and BPA (10 mg L^{-1}) was prepared under an ultrasonic water bath for 5 min and magnetically stirred in darkness for 60 min to attain adsorption/desorption equilibrium. After equilibrium, the LED lamp was switched on. At designated time intervals, aliquots of the solution were filtered using cellulose acetate syringe membrane filters (Iwaki, 0.45 μm) and subsequently analyzed using a high-performance liquid chromatograph (HPLC, PerkinElmer Series200). The HPLC analysis was carried out using an Inertsil ODS-3 column and a Series 200 UV/Vis detector at 225 nm with acetonitrile and water (70/30, v/v) as the mobile phase at a flow rate of 1 mL min^{-1}. The total organic carbon (TOC) remaining in the solution was measured using a Shimadzu ASI-V TOC analyzer. The effects of photocatalyst dosage, light sources, initial BPA concentration and various aqueous matrix anions on the photocatalytic degradation of BPA were also investigated.

Langmuir–Hinshelwood model as shown in Eq. (2) was introduced to study the photodegradation kinetics of BPA in aqueous TiO$_2$ suspension:

$$r = -\frac{dC}{dt} = \frac{kKC}{1 + KC} \tag{2}$$

where r is the reaction rate (mg L^{-1} min^{-1}), C is the concentration of pollutants (mg L^{-1}), t is the reaction time (min), k is the Langmuir–Hinshelwood reaction rate constant (mg L^{-1} min^{-1}), and K is the Langmuir adsorption equilibrium constant (L mg^{-1}). At a low BPA concentration, the pseudo-first-order kinetics model can be assumed as shown in Eqs. (3) and (4):

$$r = -\frac{dC}{dt} = kKC \tag{3}$$

$$\ln\left(\frac{C}{C_0}\right) = -kKt = -k_{app}t \tag{4}$$

where k_{app} is the apparent rate constant (min^{-1}) and C_0 is the initial BPA concentration after adsorption/desorption equilibrium in dark (mg L^{-1}).

3. Results and discussion

3.1. Characteristics of Fe/Er–TiO$_2$

Fig. 2 presents the XRD spectra of the as-synthesized photocatalysts. The characteristic peak at $2\theta = 25.3°$ corresponding to the anatase phase was observed for all the samples calcinated at 400–600 °C. Moreover, as compared to the pristine TiO$_2$(450), this peak is broader and weaker for the Fe or/and Er containing samples. On the other hand, with the increase of calcination temperature, the diffraction peak of anatase at 25.3° of the samples appears stronger and sharper but does not shift, indicating that better crystallites were formed. The transformation of anatase to rutile was not observed at the [CT] lower than 600 °C. The anatase crystallite sizes of all the samples determined using Scherrer equation are listed in Table 2. It has been reported that a weak peak at 30.5° was found in the spectra of Fe–TiO$_2$, which suggested the presence of ferric pseudobrookite Fe$_2$TiO$_5$ [22,27]. However, it was not found in this study. Moreover, no other diffraction peaks of the Er crystals were observed in this study, demonstrating that Er^{3+} doping in the hydrothermal synthesis has no significant effects on the crystallite phase of TiO$_2$.

The chemical states of the as-synthesized photocatalysts (Fig. 3a) were investigated by the XPS measurements. It is clear that the C 1s peaks weaken with the increasing temperature,
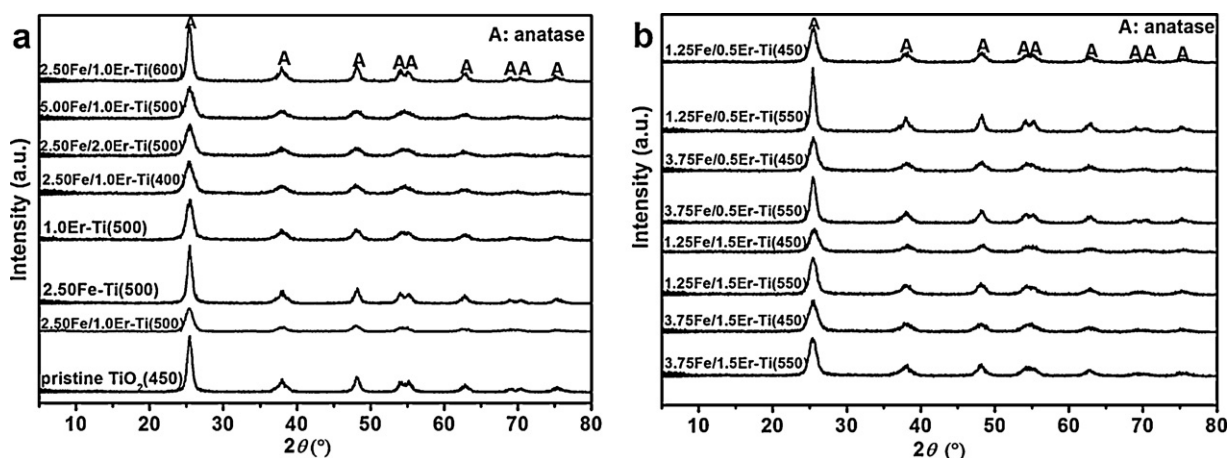

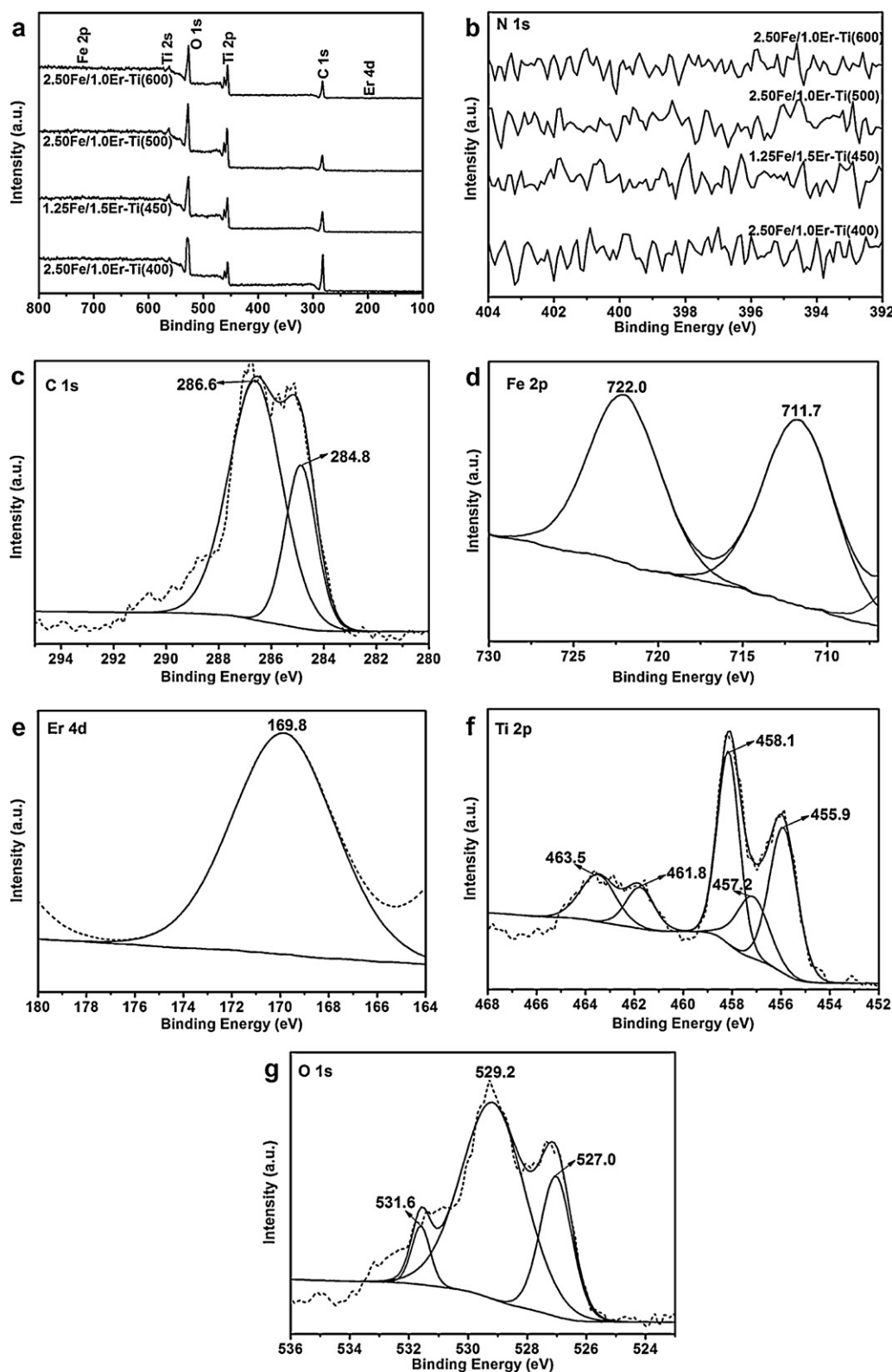**Fig. 2.** XRD spectra of synthesized photocatalysts.

Fig. 3. Survey scan XPS spectra (a) and N 1s (b) for derived photocatalysts, high-resolution XPS spectra of C 1s (c), Fe 2p (d), Er 4d (e), Ti 2p (f) and O 1s (g) for 1.25Fe/1.5Er–Ti(450).

indicating a decrease of carbon contents in TiO_2, which is corresponding to the TG analysis (Fig. 7). Moreover, as shown in Fig. 3b, no N 1s peaks was observed in the XPS analysis, indicating no nitrogen (from nitrate dopant sources) doping into the TiO_2 lattice when [CT] was higher than 400 °C. Fig. 3c shows two C 1s peaks at 284.8

and 286.6 eV. The C 1s peak at 284.8 eV is usually ascribed to the carbon residues from the organic precursor (mainly C—C bonds) [37,38], while the C 1s peaks at 286.6 eV is assigned to the carbonate species C—O bond [38]. The carbonate species were reported to function as photosensitizer, which could induce the visible-light
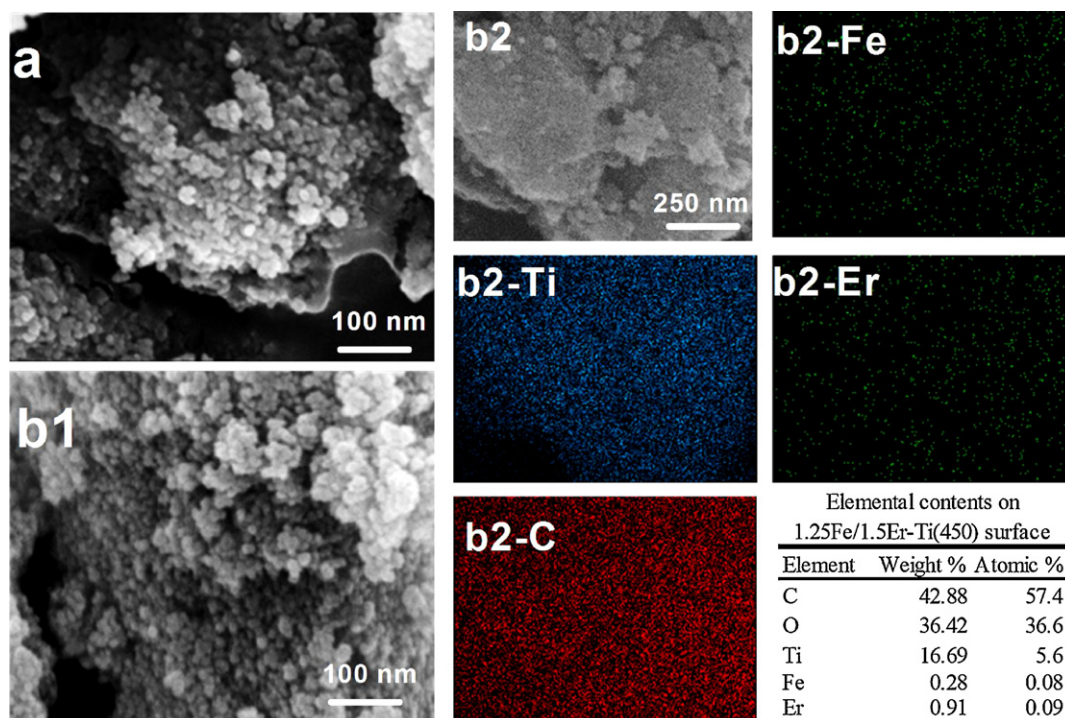
Fig. 4. SEM images of (a) the pristine TiO_2(450), and (b)1.25Fe/1.5Er–Ti(450) with element distributions maps of Ti (b2-Ti), C(b2-C), Fe(b2-Fe), Er(b2-Er) and elemental contents (inset Table).

absorption and enhance the visible-light photocatalytic activity [24,39]. In addition, the peak at around 282 eV for Ti—C bond was not found, indicating the non-existence of carbon substitutional doping in the form of Ti—C bonds [37,38]. Furthermore, Fe 2p XPS spectrum of the sample (Fig. 3d) shows the two peaks at 722.0 and 711.7 eV, corresponding to Fe $2p_{1/2}$ and Fe $2p_{3/2}$, respectively, which indicates the presence of Fe^{3+} oxidation state [40]. Moreover, the Fe $2p_{3/2}$ from the Fe modified TiO_2 shows slightly higher binding energies as compared to typical Fe $2p_{3/2}$ from Fe_2O_3 (709.8 eV) [40], which might be caused by the existence Ti–O–Fe bonds [41]. The binding energy of Er $4d_{5/2}$ (Fig. 3e) increased to 169.8 eV, whereas the binding energy was reported to be 168.0 eV in erbium oxide [43], which might be attributable to the linkage of Ti–O–Er due to the replacement of Ti sites by Er [42]. The XPS spectrum of Ti 2p is shown in Fig. 3f. Best fit of the Ti 2p envelope consist two peaks at 463.5–461.8 eV for Ti $2p_{3/2}$ and three peaks at 458.1–455.9 eV for Ti $2p_{1/2}$. The peaks at 463.5 eV for Ti $2p_{3/2}$ and 458.1 eV for Ti $2p_{1/2}$ can be assigned to TiO_2 [43,44]. The other two pairs of Ti 2p peaks of lower binding energies 457.2 and 455.9 eV in Fe/Er–TiO_2, can be attributed to Ti–O–Fe and/or Ti–O–Er linkages induced by the incorporation of Fe^{3+} and Er^{3+} into TiO_2 lattice at least at the surface [23,41]. Fig. 3g demonstrates that peaks at 529.2 and 531.6 eV were observed in the sample, which are ascribed to the Ti—O bonds in the TiO_2 lattice [45], and the surface hydroxyls (H—O bonds) [46] or/and the carbonate species [45], respectively.

The SEM micrograph coupled with the elemental mapping spectra for the pristine TiO_2(450) and 1.25Fe/1.5Er–Ti(450) are shown in Fig. 4. It is evident that all the dopant elements, including Fe and Er, were observed on the surface of the modified TiO_2. The detected atomic ratios (inset table in Fig. 4) correspond with the synthesis molar ratios (Table 2). Meanwhile, the fact that C element was noticeable indicates that the carbon contents still existed on the surface of the photocatalyst after 4 h calcination at 450 °C. This was confirmed by the XPS (Fig. 3) and TG analysis (Fig. 7).

Both the pristine TiO_2(450) and 1.25Fe/1.5Er–Ti(450) exhibited type IV isotherm with a H2 type hysteresis loop according

to the IUPAC classification (Fig. 5), indicating the presence of mesopores structures of the prepared photocatalysts. The derived S_{BET}, pore diameter (d_p) and pore volume (V_p) of photocatalysts are listed in Table 2. In general, most of the Fe/Er–TiO_2 possessed larger S_{BET} (103.40–178.20 $m^2 g^{-1}$) than the pristine TiO_2 (94.91 $m^2 g^{-1}$), while the S_{BET} of samples notably decreased with the increase of calcination temperature. In addition, from the inset of Fig. 5, it can be found that the pore diameter distribution was mainly centered at 5.6 nm for both pristine and doped TiO_2.

Fig. 6 shows the DRS in the wavelength range of 350–800 nm of the as-prepared photocatalysts. It is obvious that the doping could lead to the remarkable red shift of absorption edge of Fe/Er–TiO_2. It was ever reported that the pristine TiO_2(450) prepared by the same method exhibited the enhanced absorption of visible light
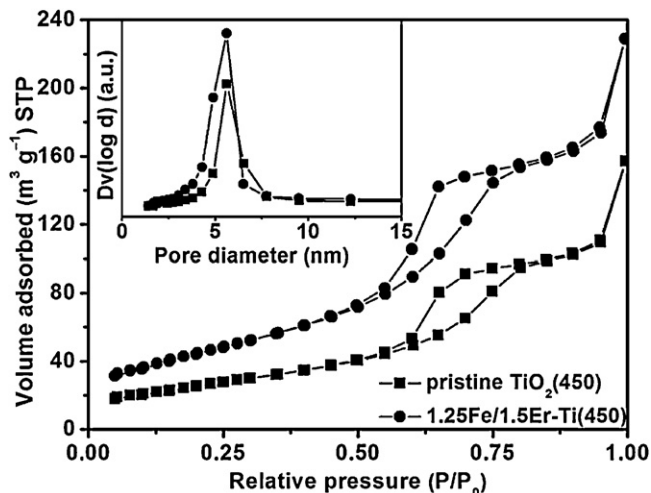

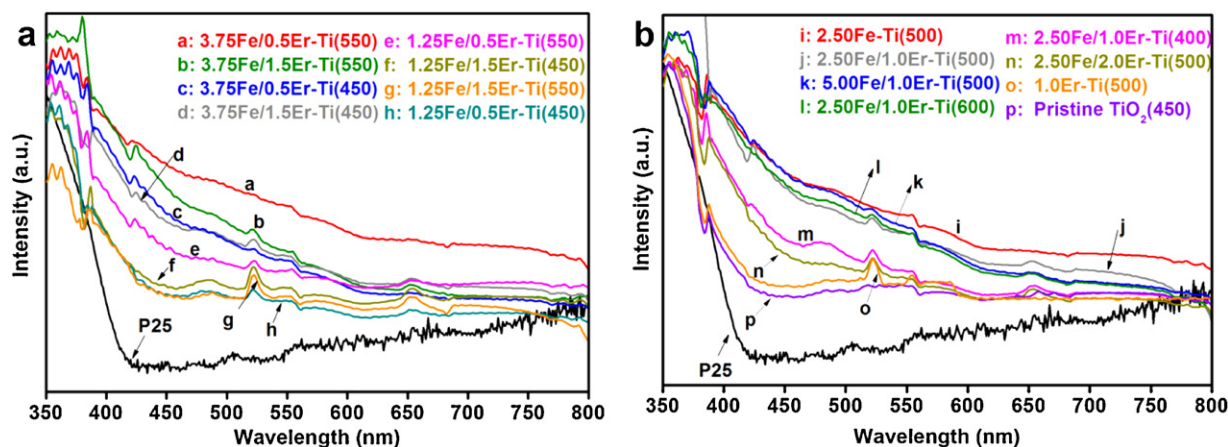**Fig. 5.** Nitrogen adsorption/desorption isotherms and pore size distributions (inset).

Fig. 6. DRS spectra of synthesized photocatalysts.

as compared to Degussa P25(P25), which could be attributed to the presence of carbonate species on the surface [22]. The introduction of Fe for Fe/Er–TiO$_2$ further caused a significant red shift of absorption edge to the visible light region in comparison to pristine TiO$_2$(450). The absorption of visible light (400–650 nm) was enhanced with the increasing [Fe] in TiO$_2$. It has been widely accepted that Fe^{3+} doping in the TiO$_2$ lattice can extend photoresponse of TiO$_2$ into visible light range for the additional electronic states within the band gap [47,48] or the narrowing of the band gap of pristine TiO$_2$ [49]. Moreover, it is seen from the comparison of the pristine TiO$_2$(450) and 1.0Er–Ti(500) that the doping of Er^{3+} does not cause much change in the absorption edge of TiO$_2$, indicating that Er^{3+} doping has no significant effects on the crystallites phase of TiO$_2$, which is in good agreement with XRD results (Fig. 2). Compared with P25 and the pristine TiO$_2$(450), two absorption peaks centered at 523 and 654 nm were observed for Er^{3+} doped TiO$_2$. This could be assigned to the upconversion energy transitions from the $^4I_{15/2}$ ground state to $^2H_{11/2}$ and $^4F_{9/2}$ states of Er^{3+}, respectively [23,50].

Fig. 7 shows the weight loss profile of the 1.25Fe/1.5Er–Ti(450) precursor dried at 80 °C during heating in the air, while Fig. S1 (Supporting Information) shows the FT-IR spectra of the gaseous species evolved from the TG analysis at different temperatures. The distinct step at 44–124 °C in TG curve could be attributed to the loss of surface-adsorbed water or/and CO$_2$ molecules. The peak corresponding to 124–281 °C in DTG curve might be attributed to the

decomposition of carbon species. The major weight loss of 11.9% occurred below 300 °C, the subsequent weight loss of 1.9% happened at 300–600 °C, and the stable weight of sample could be observed at 620 °C and above. The minor decrease of weight at 300–600 °C might be resulted from the loss of small amount of carbon species, from TTIP or/and IP, doped in TiO$_2$.

Fig. 8 shows the PL spectra of the pristine TiO$_2$(450) and Er^{3+} or/and Fe^{3+} doped TiO$_2$. There observed a significant decrease in the intensity of PL spectra of 1.25Fe/1.5Er–Ti(450) compared to that of the pristine TiO$_2$(450), 1.5Er–Ti(450), 1.25Fe–Ti(450) and 1.25Fe/0.5Er–Ti(450). It implies that TiO$_2$ codoping with Fe and Er restrained the recombination of photo-induced electrons and holes effectively. The effective inhibition of e$^-$/h$^+$ recombination for 1.25Fe/1.5Er–Ti(450) could improve its visible-light photocatalytic performance effectively.

3.2. RSM model analysis

The CCD matrix coupled with the experimental and predicted results of BPA degradation efficiencies after 4 h LED-W irradiation using the prepared photocatalysts are presented in Table 2. A second-order polynomial expression in Eq. (5) consisting of 10 coefficients was obtained from the analysis of variance (ANOVA) at 95% confidence level ($p < 0.05$). The sum of squares, mean squares, estimated coefficient, standard error, and the corresponding F-value and p-values were also tested using ANOVA, and the
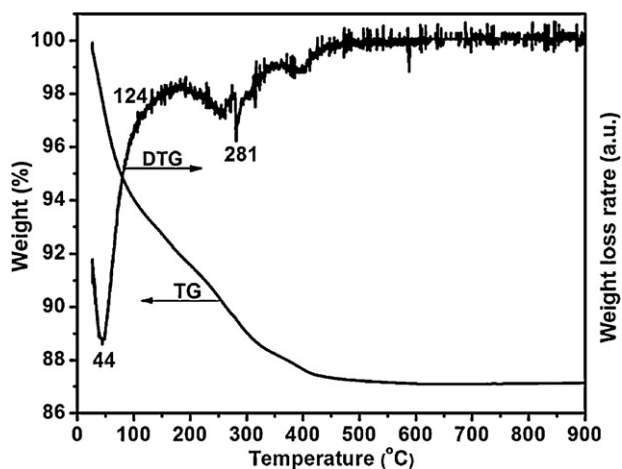

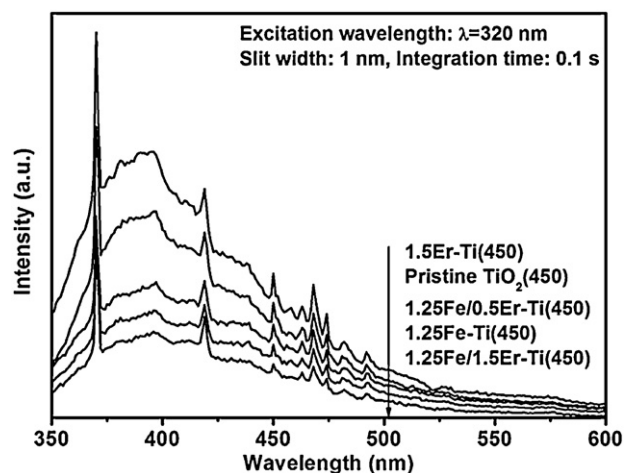**Fig. 7.** TG/DTG profiles of the 1.25Fe/1.5Er–Ti(450) precursor dried at 80 °C.

Fig. 8. PL spectra of derived photocatalysts.

Table 3
ANOVA results for response surface quadratic model for 4 h PCD of BPA.

Source of variations	Sum of squares	Mean square	Parameter estimate	Coefficient estimate	Standard error	F-value	p-Value
Model	5934.04	659.34	–	–	–	28.74	<0.0001
Intercept	–	–	−143.26	86.29	1.97	–	–
[Er]	44.56	44.56	−49.42	1.67	1.24	1.94	0.1936
[Fe]	3314.88	3314.88	50.38	−14.39	1.24	144.50	<0.0001
[CT]	1618.05	1618.05	1.02	−10.06	1.24	70.53	<0.0001
[Er][Fe]	116.28	116.28	−6.10	−3.81	1.75	5.07	0.0481
[Er][CT]	136.95	136.95	0.17	4.14	1.75	5.97	0.0347
[Fe][CT]	245.31	245.31	−0.09	−5.54	1.75	10.69	0.0084
$[Er]^2$	85.42	85.42	−7.37	−1.84	0.99	3.72	0.0825
$[Fe]^2$	324.62	324.62	−2.30	−3.59	0.99	14.15	0.0037
$[CT]^2$	212.28	212.28	−9.1E−3	−2.91	0.99	9.25	0.0124
Residual	229.41	22.94	–	–	–	–	–
Lack of fit	229.03	45.81	–	–	–	613.48	<0.0001
Pure error	0.37	0.07	–	–	–	–	–

$R^2 = 0.963$, adjusted $R^2 = 0.929$, adequate precision = 17.00.

results are summarized in Table 3. In statistics, a model with a large F-value and a small p-value (<0.05) is considered to be significant [51].

$$BPA\,removal(\%) = -143.26 - 49.42[Er] + 50.38[Fe] + 1.02[CT]$$
$$- 6.10[Er][Fe] + 0.17[Er][CT] - 0.09[Fe][CT]$$
$$- 7.37[Er]^2 - 2.30[Fe]^2 - 9.1 \times 10^{-3}[CT]^2 \quad (5)$$

It is observed in the ANOVA test that for the first-order and second-order main effects, i.e., [Fe], $[Fe]^2$, [CT] and $[CT]^2$ are more highly significant than [Er] and $[Er]^2$. Moreover, in terms of interactive effects, [Fe][CT] is more significant than [Er][CT] and [Er][Fe]. On the other hand, the coefficients of [Fe], [CT] and [Er][CT] indicate positive influences on BPA degradation, while [Er], [Er][Fe], [Fe][CT], $[Er]^2$, $[Fe]^2$ and $[CT]^2$ indicate negative influences.

The ANOVA reveals that Eq. (5) ($R^2 = 0.929$) suitably explains the actual relationship between the response and the variables, which can be seen in Fig. 9 by comparing the experimentally measured values against the predicted responses for the BPA removal efficiency. As shown in the inset of Fig. 9, a random distribution was observed for the residual plots for the models and dataset on BPA removal efficiency, indicating that the residual distribution of the regression equation follows normal and independent patterns [52]. This suggests a high adequacy of the quadratic models. In addition, a very low probability value ($p < 0.0001$) obtained from the Fisher

F-test demonstrates a very high significance for the second-order equation in this study.

To confirm the validity of the statistical experimental strategies, three confirmation experiments were conducted. The synthesis conditions, experimental and predicted results are listed in Table 4. The measured values of BPA removal efficiencies after 4 h LED-W irradiation were found to be very close to those estimated using the RSM model.

The three-dimensional response surface and two-dimensional contour plots as an estimate of BPA removal efficiency are constructed and shown in Fig. 10. These are graphical representations of Eq. (5) and they also show the interactions among [Er], [Fe] and [CT]. The elliptical shape of the contour plot in Fig. 10a-2 indicates a significant interaction between [Er] and [Fe] [52,53]. The elliptical counter plots shown in Fig. 10b-2 and c-2 also indicate strong [Er][CT] and [Fe][CT] interactions.

In Fig. 10a-2, the contour plot is developed as a function of [Er] and [Fe] with [CT] fixed at 450 °C. As can be seen, at a lower [Fe] (<3 mol%), BPA removal efficiency increases with [Er] until its optimum concentration beyond which the BPA removal efficiency starts to decrease. This can be explained by the two possible upconversion processes: excited state absorption (ESA) process and energy transfer upconversion (ETU) process in the Er^{3+} doped hosts [17,18,42]. ESA is a single ion process which is independent of [Er], while ETU process involves two ions. When the [Er] is low, the interactions between two Er^{3+} ions are negligible due to the random distribution of Er^{3+} ions around the host lattice. The ESA becomes the dominant upconversion process, and the upconversion capability of the photocatalyst is enhanced with the increasing [Er] [42]. At a higher [Er], ETU becomes the dominant process due to the increased proximity among Er^{3+} ions. At excessively high [Er] (e.g., >1.5 mol%), Er^{3+}(1.03 Å) clusters may form outside the Ti^{4+}(0.68 Å) lattice, leading to self-quenching which is detrimental to the whole upconversion efficiency [23]. With respect to [Fe], BPA removal efficiency first increases with [Fe] but then decreases with further increasing [Fe] beyond its optimum concentration (when [Er] is lower than 1.5 mol%). The suggested increase in photoactivity could be caused by the incorporation of Fe into the TiO_2 lattice which
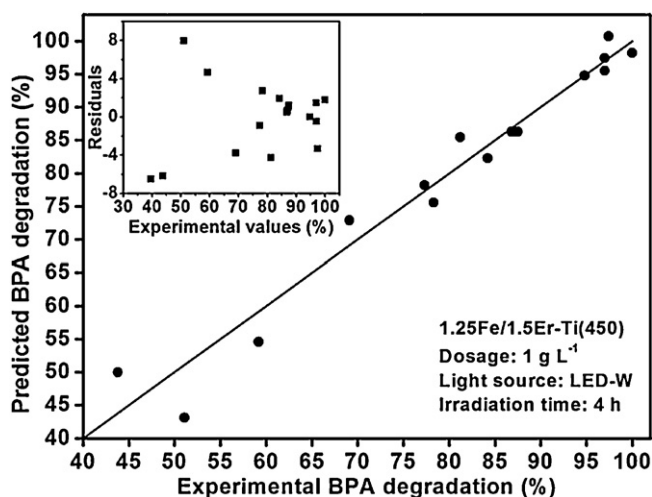
Fig. 9. The experimental BPA degradation (%) plotted against the predicted values derived from the RSM model (inset shows residual plots of quadratic model).

Table 4
Results of confirmation experiments.

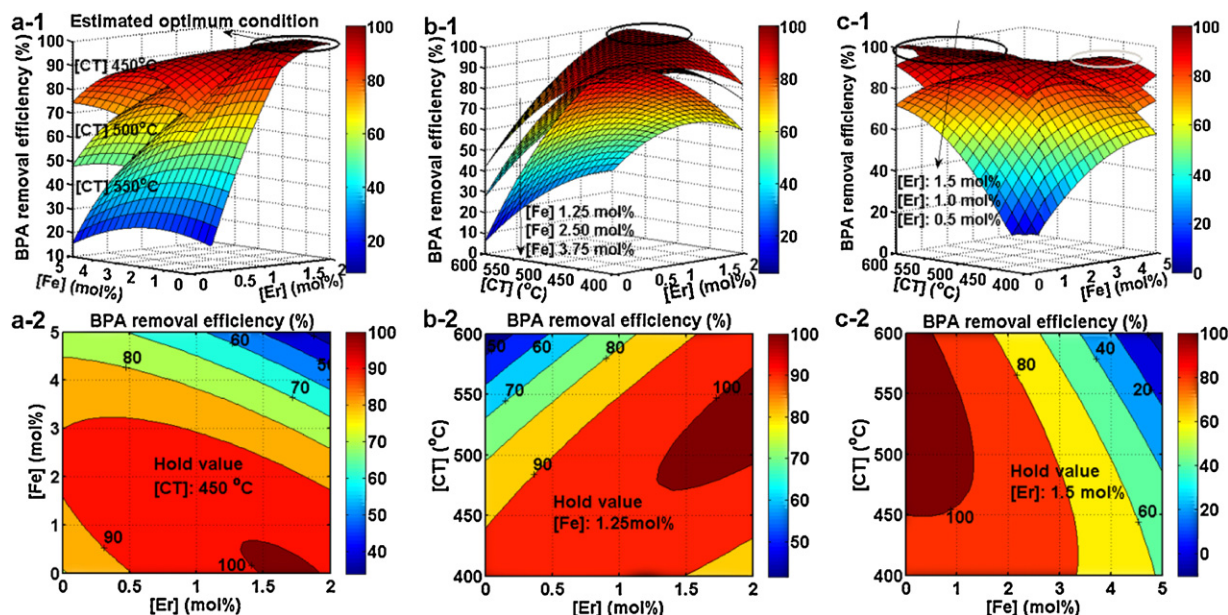| Trial	[Er] (mol%)	[Fe] (mol%)	[CT] (°C)	BPA degradation (%)	
				Measured	Calculated
1	0	0	450	82.6	79.1
2	0	1.25	450	91.3	88.6
3	1.5	0	450	97.0	100

Fig. 10. Surface (1) and contour (2) plots for BPA removal (%) under LED-W irradiation for 4 h with a dosage of 1 g L^{-1}. (a) X_1 ([Er]) and X_2 ([Fe]) in fixed X_3 ([CT]), (b) X_1 ([Er]) and X_3 ([CT]) in fixed X_2 ([Fe]), (c) X_2 ([Fe]) and X_3 ([CT]) in fixed X_1 ([Er]).

not only enhances the absorption ability of visible light, but also suppresses recombination of photo-induced electrons and holes of TiO$_2$ [14,54]. However, Fe^{3+} dopant with a high concentration could function as the recombination centers for the photogenerated e$^-$/h$^+$ [14,28]. In addition, it is also obvious that when [Fe] is higher than 3 mol% or [Er] higher than 1.5 mol%, BPA removal efficiency decreases with the increasing [Er] or [Fe], respectively. This might be attributable to the similar ion radii of Ti^{4+}(0.68 Å) and Fe^{3+}(0.64 Å), so that the Er^{3+}(1.03 Å) ions could occupy the outer site of the lattice and interact with Fe^{3+} to form Er–O–Fe linkage which could undermine the upconversion luminance process of Er^{3+} [55].

In Fig. 10b-2, the contour plot is developed as a function of [Er] and [CT] with [Fe] fixed at 1.25 mol%. As can be seen, when [CT] is lower than 500 °C, BPA removal efficiency first increases and then decreases with the increasing [Er], which can also be well explained by the ESA process and ETU process. When [CT] is increased to 600 °C, the TiO$_2$ phase does not change and the crystallite size grows to more than 10 nm (Table 2). Due to the increased crystallite size, the TiO$_2$ lattice could provide more sites for Er^{3+}. ESA dominants the upconversion process and the photocatalysis of TiO$_2$ is enhanced with the increasing [Er]. Moreover, as shown in Fig. 10b-2, at a low [Er] (<0.5 mol%), BPA removal efficiency decreases with the increasing calcination temperature. The decrease in photoactivity shall be caused by the loss of C contents (e.g. C–O and C=O) in TiO$_2$ lattice (Fig. 3). It is postulated that the lattice defects arising from the C modification would be critical for the visible-light photocatalysis. The lattice impurities could inhibit recombination of the photoinduced electrons and holes, leading to the increased photonic efficiency [56]. However, at a high [Er] (>1.0 mol%), BPA removal efficiency first increase and then decreases with further increasing the calcination temperature. The increase in photoactivity (indicated by k_{app} in Tables 2 and 5) might be attributed to the increased crystallite size and enhanced nanocrystallinity for TiO$_2$ due to the increased [CT] (Table 2). This not only enhances the upconversion luminance capability [42,57], but also strengthens the absorption ability of visible light [45]. However, at a higher temperature, the positive effects are overwhelmed by the decrease in photoactivity caused by the loss of C contents in TiO$_2$ lattice.

All in all, the interactive effects between [Er], [Fe] and [CT] resulted in two possible optimum synthesis conditions of Fe/Er–TiO$_2$ (Fig. 10c-1): (1) 0.5–1.0 mol% [Er], 2.0–3.0 mol% [Fe] and 400–450 °C [CT], and (2) 1.5–2.0 mol% [Er], 0–1.5 mol% [Fe] and 450–600 °C [CT]. Based on our experimental k_{app} values (Table 2), we set the optimum condition to be at 1.5 mol% [Er], 1.25 mol% [Fe] and 450 °C [CT].

3.3. Photocatalytic degradation of BPA

Photolysis of BPA throughout the 4 h LED-W irradiation was negligible (Fig. 11a). Generally, the synthesized Fe/Er–TiO$_2$ via solvothermal method showed enhanced photocatalytic BPA degradation compared to that of P25 under visible light (Tables 2 and 5). It is postulated that the lattice defects induced by the Fe and Er dopants or/and carbonate species were responsible for the visible-light photocatalytic activities of these photocatalysts.

3.3.1. Effect of dopants

Fig. 11a shows the PCD of BPA with various synthesized photocatalysts and P25 under LED-W irradiation at neutral pH. The corresponding k_{app} values are summarized in Table 5. It is obvious that the as-synthesized pristine TiO$_2$, 1.25Fe–Ti(450) and 1.5Er–Ti(450) all exhibited significantly improved PCD efficiencies compared to that of P25. In particular, 1.25Fe/1.5Er–Ti(450), combining the synergistic effects of photosensitizing (C–O band), narrowed band gap and enhanced e$^-$/h$^+$ separation (Ti–O–Fe linkage), and upconversion luminescence property (Ti–O–Er linkage), showed a further enhanced photocatalytic activity over any of the other as-synthesized photocatalysts. BPA (10 mg L^{-1}) was completely degraded by the Fe/Er–TiO$_2$ (1.0 g L^{-1}) after 4 h of visible light irradiation, corresponding to 75% of TOC mineralization.

3.3.2. Effect of TiO$_2$ dosage

It can be seen from Fig. 11b that the photocatalytic degradation efficiencies increase with the dosage of Fe/Er–TiO$_2$ up to 1.0 g L^{-1} with a corresponding k_{app} value of 21.8×10^{-3} min^{-1} (Table 5). Increase of the dosage from 0.50 to 1.0 g L^{-1} led to a 25% increase of k_{app} value, while higher dosages (>1.0 g L^{-1}) resulted in

Table 5
k_{app} and r_o values of BPA photocatalytic degradation under various experimental conditions.

TiO$_2$	C_I [a] (mg L^{-1})	C_0 [b] (mg L^{-1})	Dosage (g L^{-1})	Light source	Anion	k_{app} [c] (min^{-1}), 10^{-3}	r_o [d] (mg L^{-1} min^{-1}), 10^{-3}
P25	10	5.19	1.0	LED-W		5.4(0.949 [e])	27.9
Pristine TiO$_2$(450)		6.00				8.4(0.971)	50.5
1.25Fe–Ti(450)		5.41				10.8(0.962)	58.4
1.5Er–Ti(450)		5.60				15.3(0.972)	85.7
1.25Fe/1.5Er–Ti(450)		5.45				21.8(0.926)	118.6
1.25Fe/1.5Er–Ti(450)	10	6.22	0.5	LED-W		17.4(0.942)	108.0
		5.45	1.0			21.8(0.926)	118.6
		5.05	1.5			22.0(0.902)	111.2
		4.61	2.0			22.8(0.917)	105.3
1.25Fe/1.5Er–Ti(450)	10	5.45	1.0	LED-W		21.8(0.926)	118.6
		5.57		LED-B		15.6(0.959)	86.8
		6.05		LED-G		1.3(0.944)	7.7
		6.41		LED-Y		1.7(0.855)	10.7
		6.18		LED-R		0.7(0.933)	4.3
		6.41		SV		9.4(0.982)	60.0
1.25Fe/1.5Er–Ti(450)	10	5.45	1.0	LED-W		21.8(0.926)	118.6
	20	10.26				17.1(0.901)	175.7
	30	18.65				14.6(0.929)	272.0
	50	30.10				11.3(0.944)	341.0
1.25Fe/1.5Er–Ti(450)	10	5.45	1.0	LED-W		21.8(0.926)	118.6
		6.35			Cl$^-$	19.9(0.941)	126.2
		5.84			SO$_4^{2-}$	18.5(0.907)	108.2
		5.24			NO$_3^-$	16.3(0.880)	85.4
		6.52			HCO$_3^-$	6.7(0.972)	44.0
		5.68			Tap	4.2(0.906)	23.8

[a] Initial pollutants concentration.
[b] Initial concentration after adsorption/desorption equilibrium in dark.
[c] Apparent rate constant.
[d] Initial degradation rate.
[e] R^2, correlation of determination.

insignificant increases of k_{app}. Obviously, with the increase of TiO$_2$ dosage, the photocatalyst surface area available for adsorption and photocatalytic degradation was increased, but the increased solution opacity could negate such beneficial effects. The plot of initial degradation rate (r_0) as a function of dosage is shown in the inset of Fig. 11b, which indicates that the optimum photocatalyst dosage was 1.0 g L^{-1}.
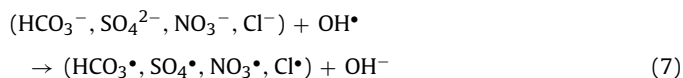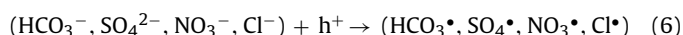
3.3.3. Effect of light sources

As shown in Fig. 11c, the degradation efficiencies of BPA by 1.25Fe/1.5Er–Ti(450) after 3 h of LED-W, B, G, Y, R and SV irradiations are 98%, 91%, 21%, 23%, 11% and 81% with k_{app} values of 21.8, 15.6, 1.3, 1.7, 0.7 and 9.4×10^{-3} min^{-1}, respectively. Apparently, the BPA degradation efficiency is higher under LED-W, B and SV irradiations than under LED-G, Y and R irradiations. Moreover, a fraction of BPA was also removed under LED-G, Y and R irradiations, showing that 1.25Fe/1.5Er–Ti(450) could be photoexcited by the full spectrum of visible light. These findings confirmed the red shift of absorption edge of 1.25Fe/1.5Er–Ti(450) as shown in Fig. 6.

3.3.4. Effect of initial BPA concentration and degradation kinetics

Fig. 11d illustrates the effect of initial BPA concentration on its photocatalytic degradation and the kinetics. The k_{app} value decreases from 21.8 to 11.3×10^{-3} min^{-1} as the initial BPA concentration increases from 10 to 50 mg L^{-1} (Table 5). The decreasing k_{app} values can be ascribed to the increasing light absorption by the BPA molecules rather than TiO$_2$. The increasing competition between the BPA molecules (and its degradation byproducts) for adsorption and reaction with the generated radicals on TiO$_2$ surfaces could also affect BPA degradation. The linear plot of Langmuir–Hinshelwood model (Eq. (2)) is shown in the inset of Fig. 11d. The Langmuir–Hinshelwood reaction rate constant and Langmuir adsorption equilibrium constant are 0.554 mg L^{-1} min^{-1} and 0.049 L mg^{-1} ($R^2 = 0.989$), respectively.

3.3.5. Effect of anions

The anions investigated generally exhibited varying degrees of inhibitory effects on photocatalytic activities of 1.25Fe/1.5Er–Ti(450), with the orders of significance following bicarbonate > sulfate > nitrate > chloride at 1.0 mM (as shown in Table 5 and Fig. 11e). This was due to the fact that the anions could scavenge h$^+$ or/and OH$^\bullet$ to form ionic radicals (Eqs. (6) and (7)) [58] which are less reactive than h$^+$ and OH$^\bullet$. Therefore, the presence of anions would inhibit the BPA degradation. In addition, the tap water which contains trace concentrations of various cations and anions (Table S1) showed the largest inhibition on the photocatalytic degradation process. Therefore, the effects of ions should be considered in the application of photocatalysis in treating the real water and wastewater.

$$(HCO_3^-, SO_4^{2-}, NO_3^-, Cl^-) + h^+ \rightarrow (HCO_3^\bullet, SO_4^\bullet, NO_3^\bullet, Cl^\bullet) \quad (6)$$

$$(HCO_3^-, SO_4^{2-}, NO_3^-, Cl^-) + OH^\bullet$$
$$\rightarrow (HCO_3^\bullet, SO_4^\bullet, NO_3^\bullet, Cl^\bullet) + OH^- \quad (7)$$

3.3.6. Photocatalyst stability

Fig. 11f shows the durability of 1.25Fe/1.5Er–Ti(450) for BPA degradation under LED-W irradiation. In a typical procedure after a 4 h PCD experiment, the photocatalyst was recovered by simple centrifugation, washed with DI water and reused without further treatment. The reduction of visible-light photocatalytic activity was insignificant even after ten cycles, indicating a good physicochemical stability of the synthesized Fe/Er–TiO$_2$ via the solvothermal method under the experimental conditions of this study.

3.4. Proposed mechanism

In order to identify the possible mechanisms of photocatalytic degradation of BPA, different chemical probes were used to scavenge the reactive oxygen species generated from visible-light
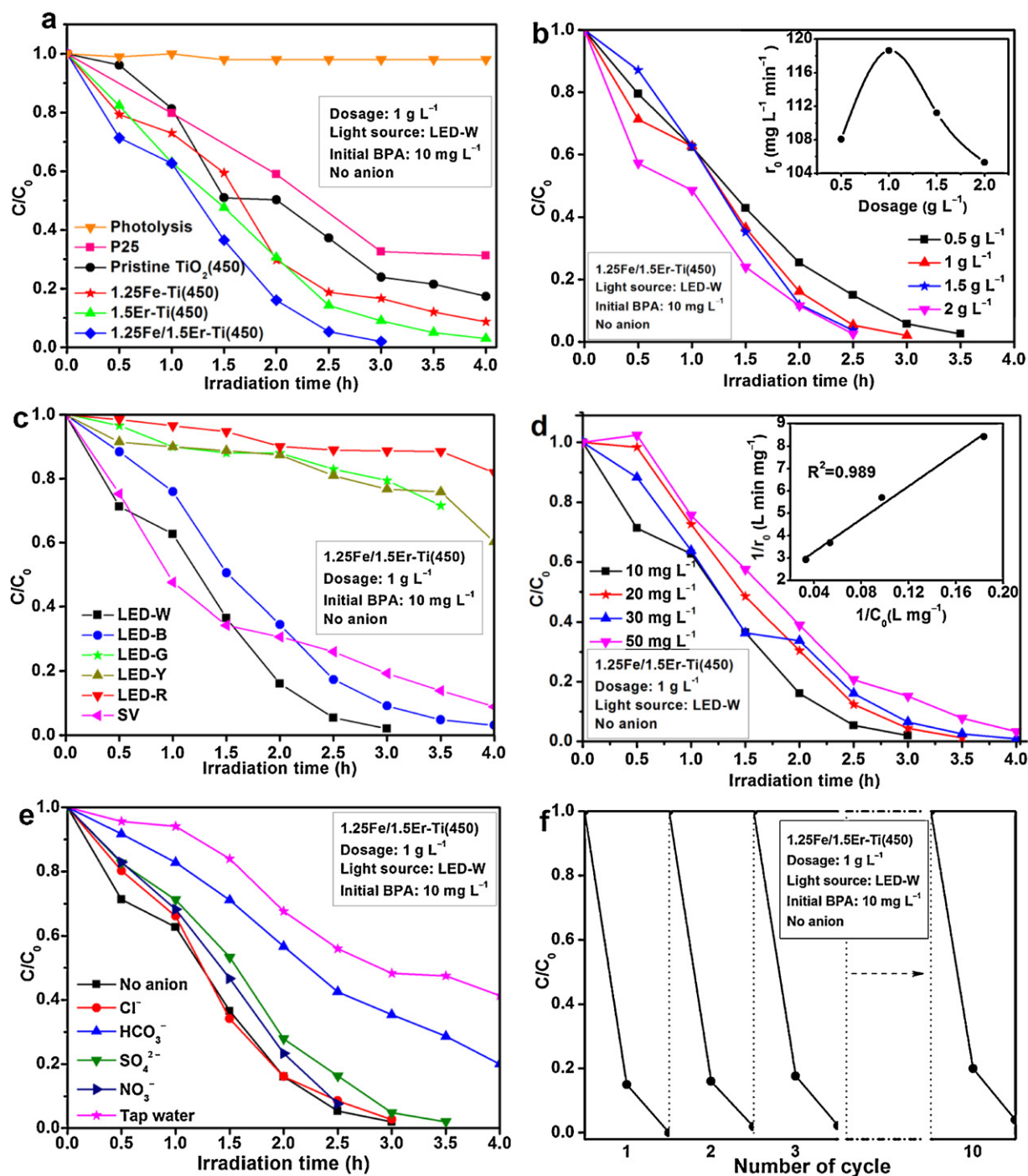
Fig. 11. Effect of (a) dopants, (b) dosage (inset shows initial degradation rate versus dosage), (c) light sources, (d) initial BPA concentration (inset shows linear plot fitting of Langmuir–Hinshelwood model), (e) 1.0 mM anion, (f) recycling use on photocatalytic degradation of BPA.

photocatalysis and to observe their effects on BPA degradation. The chemical probes used were potassium iodide (KI), dimethyl sulfoxide (DMSO), benzequione (BQ) and sodium azide (NaN$_3$) which are the scavengers of photogenerated h$^+$, hydroxyl radical (OH$^\bullet$), superoxide radical (O$_2^{\bullet-}$) and singlet oxygen (^{1}O$_2$), respectively. The findings are presented in Supporting Information (Fig. S2 and its discussion). The proposed photocatalytic mechanism of Fe/Er–TiO$_2$ under visible light irradiation is shown in Fig. 12.

The UV (326–342 and 354–359 nm), violet (405–420 nm), blue (436–442 nm) and green (525–575 nm) upconversion luminescence were simultaneously observed in Er^{3+}:YAlO$_3$ under 652.2 nm excitation [17,18,23]. This means that for the role of the Ti–O–Er

linkages, the upconversion reagent Er^{3+} can be easily excited by visible light as excitation source and then emits UV or/and the short-wavelength visible light which may photoexcite the Fe/Er–TiO$_2$. In addition, the upconversion process in the Er^{3+} doped TiO$_2$ nanoparticles depends not only on the Er^{3+} concentration [17,23,42] but also on the TiO$_2$ crystallite phase [42] and size [57].

For the role of carbonate species (C—O bonds) in the visible-light photocatalytic ability of the Fe/Er–TiO$_2$, some studies have demonstrated that carbonate species assigned to interstitial carbon dopant could act as photosensitizer. It can be excited under visible light irradiation and then inject its e$^-$ into the conduction band (CB) of TiO$_2$. Subsequently, the e$^-$ are transferred to the adsorbed O$_2$ on
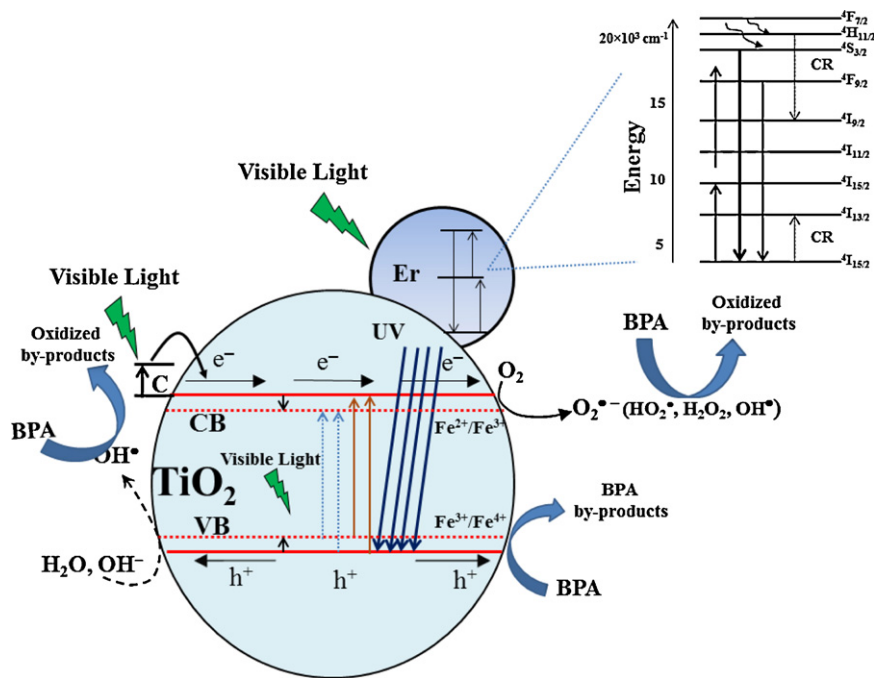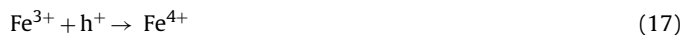
Fig. 12. Proposed photocatalytic mechanisms over the Fe/Er–TiO$_2$ under visible light irradiation.

the TiO$_2$ surface, producing O$_2^{\bullet-}$ and the other reactive oxidizing species which are capable of degrading organic compounds [24,25]. According to XRD, XPS and UV–vis DRS analyses, the carbonate species in the synthesized TiO$_2$ did not induce TiO$_2$ lattice distortion nor change in TiO$_2$ band gap and Ti chemical state. Moreover, the C contents would be removed via calcination at high temperatures (>400 °C).

It has been reported that Fe^{3+} doping into TiO$_2$ lattice would introduce new dopant energy levels into TiO$_2$ band gap: the Fe^{3+}/Fe^{4+} couple above the valence band (VB) [59] and the Fe^{3+}/Fe^{2+} couple below CB [48]. Under irradiation of UV (upconverted by Er) or short-wavelength visible light, e$^-$ could be photoexcited from VB (Eq. (8)) or/and from Fe^{3+}/Fe^{4+} (Eq. (11)) to CB directly. As a result, the photogenerated CB e$^-$ could further react with the adsorbed O$_2$ to form O$_2^{\bullet-}$ (Eq. (10)), while the simultaneously generated holes in the VB or/and Fe^{4+} could migrate to the surface of TiO$_2$ and react with the surface hydroxyl group to produce OH$^\bullet$ (Eqs. (9) and (12)) [59]. However, due to the existence of Fe^{3+}/Fe^{4+} and Fe^{3+}/Fe^{2+} bands, the e$^-$ might be also trapped by the bands and reduce Fe^{3+} to Fe^{2+} and produce O$_2^{\bullet-}$ (Eqs. (13) and (14)) [27]. The photocatalytic reaction could also involve the mechanistic steps shown in Eqs. (15) and (16) [22]. However, Fe^{3+} dopant at a high concentration could serve as recombination centers for the photogenerated e$^-$/h$^+$ (Eqs. (17) and (18)) [27], leading to the decreased activity of the photocatalyst.

$$TiO_2 + h\nu \rightarrow h^+ + e^- \tag{8}$$

$$h^+ + OH^- \rightarrow OH^\bullet \tag{9}$$

$$e^- + O_2 \rightarrow O_2^{\bullet-} \tag{10}$$

$$Fe^{3+} + h\nu \rightarrow Fe^{4+} + e^- \tag{11}$$

$$Fe^{4+} + OH^- \rightarrow Fe^{3+} + OH^\bullet \tag{12}$$

$$Fe^{3+} + e^- \rightarrow Fe^{2+} \tag{13}$$

$$Fe^{2+} + O_2 \rightarrow Fe^{3+} + O_2^{\bullet-} \tag{14}$$

$$Fe^{2+} + Ti^{4+} \rightarrow Fe^{3+} + Ti^{3+} \tag{15}$$

$$Ti^{3+} + O_2 \rightarrow Ti^{4+} + O_2^{\bullet-} \tag{16}$$

$$Fe^{3+} + h^+ \rightarrow Fe^{4+} \tag{17}$$

$$Fe^{4+} + e^- \rightarrow Fe^{3+} \tag{18}$$

4. Conclusions

The novel Fe/Er–TiO$_2$ combining the synergistic effects of photosensitizing (C–O band), narrowed band gap and enhanced e$^-$/h$^+$ separation (Ti–O–Fe linkage), and upconversion luminescence property (Ti–O–Er linkage), showed a superbly enhanced photocatalytic activities for BPA degradation compared to the pristine TiO$_2$, Er–TiO$_2$, Fe–TiO$_2$ and P25 under visible light irradiation. The RSM model obtained ($R^2 = 0.929$) shows a satisfactory correlation between the experimental results and predicted values of BPA removal efficiency under LED-W irradiation for 4 h. In terms of individual effects, both [Fe] and [CT] were found more significant than [Er] in affecting the BPA removal efficiency. On the other hand, for the interactive effects, [Er][CT], [Fe][CT] and [Er][Fe] were all significant. The RSM model also suggests that the optimum condition for the synthesis of Fe/Er–TiO$_2$ should be 1.5 mol%, 1.25 mol% and 450 °C for [Er], [Fe] and [CT], respectively. With Fe/Er–TiO$_2$ (1.0 g L^{-1}), BPA (10 mg L^{-1}) can be completely degraded after 4 h of visible light irradiation with 75% TOC removal. The photocatalytic activity of the Fe/Er–TiO$_2$ was maintained even after ten cycles of use indicating its high physicochemical stability of the synthesized photocatalyst.

Appendix A. Supplementary data

Supplementary data associated with this article can be found, in the online version, at http://dx.doi.org/10.1016/j.apcatb.2012.07.012.

References

[1] A.V. Krishnan, P. Stathis, S.F. Permuth, L. Tokes, D. Feldman, Endocrinology 132 (1993) 2279–2286.
[2] J. Jackson, R. Sutton, Science and Total Environment 405 (2008) 153–160.
[3] M.N. Chong, B. Jin, C.W.K. Chow, C. Saint, Water Research 44 (2010) 2997–3027.
[4] M.R. Hoffmann, S.T. Martin, W. Choi, D.W. Bahnemann, Chemical Reviews 95 (1995) 69–96.
[5] M. Iwasaki, M. Hara, H. Kawada, H. Tada, S. Ito, Journal of Colloid and Interface Science 224 (2000) 202–204.
[6] H. Irie, Y. Watanabe, K. Hashimoto, Chemistry Letters 32 (2003) 772–773.
[7] R. Bacsa, J. Kiwi, T. Ohno, P. Albers, V. Nadtochenko, Journal of Physical Chemistry B 109 (2005) 5994–6003.
[8] G.S. Wu, J.P. Wang, D.F. Thomas, A.C. Chen, Langmuir 24 (2008) 3503–3509.
[9] C. Belver, R. Bellod, A. Fuerte, M. Fernandez-Garcia, Applied Catalysis B: Environmental 65 (2006) 301–308.
[10] C. Belver, R. Bellod, S.J. Stewart, F.G. Requejo, M. Fernandez-Garcia, Applied Catalysis B: Environmental 65 (2006) 309–314.
[11] X.B. Chen, C. Burda, Journal of the American Chemical Society 130 (2008) 5018–5019.
[12] S. Klosek, D. Raftery, Journal of Physical Chemistry B 105 (2001) 2815–2819.
[13] J.B. Yin, X.P. Zhao, Chemistry of Materials 16 (2004) 321–328.
[14] Z.J. Li, W.Z. Shen, W.S. He, X.T. Zu, Journal of Hazardous Materials 155 (2008) 590–594.
[15] A.W. Xu, Y. Gao, H.Q. Liu, Journal of Catalysis 207 (2002) 151–157.
[16] J. Wang, R.H. Li, Z.H. Zhang, W. Sun, R. Xu, Y.P. Xie, Z.Q. Xing, X.D. Zhang, Applied Catalysis A: General 334 (2008) 227–233.
[17] N.N. Zu, H.G. Yang, Z.W. Dai, Physica B 403 (2008) 174–177.
[18] H.G. Yang, Z.W. Dai, Z.W. Sun, Journal of Luminescence 124 (2007) 207–212.
[19] J. Wang, Y.P. Xie, Z.H. Zhang, J. Li, X. Chen, L.Q. Zhang, R. Xu, X.D. Zhang, Solar Energy Materials and Solar Cell 93 (2009) 355–361.
[20] D.X. Hou, H. Feng, J.B. Zhang, S.S. Dong, D.D. Zhou, T.T. Lim, Journal of Hazardous Materials 199 (2012) 301–308.
[21] P.H. Wang, T. Zhou, R. Wang, T.T. Lim, Water Research 45 (2011) 5015–5026.
[22] X.P. Wang, Y.X. Tang, M.Y. Leiw, T.T. Lim, Applied Catalysis A: General 409 (2011) 257–266.
[23] T.F. Zhou, J.C. Hu, J.L. Li, Applied Catalysis B: Environmental 110 (2011) 221–230.
[24] C. Lettmann, K. Hildenbrand, H. Kisch, W. Macyk, W.F. Maier, Applied Catalysis B: Environmental 32 (2001) 215–227.
[25] X. Yang, C. Cao, K. Hohn, L. Erickson, R. Maghirang, D. Hamal, K. Klabunde, Journal of Catalysis 252 (2007) 296–302.
[26] H. Yamashita, M. Harada, J. Misaka, M. Takeuchi, K. Ikeue, M. Anpo, Journal of Photochemistry and Photobiology A 148 (2002) 257–261.
[27] M. Asilturk, F. Sayilkan, E. Arpac, Journal of Photochemistry and Photobiology A 203 (2009) 64–71.
[28] X.P. Wang, T.T. Lim, Applied Catalysis B: Environmental 100 (2010) 355–364.
[29] S.F. Zuo, Q.Q. Huang, J. Li, R.X. Zhou, Applied Catalysis B: Environmental 91 (2009) 204–209.
[30] A.F. Caliman, C. Cojocaru, A. Antoniadis, I. Poulios, Journal of Hazardous Materials 144 (2007) 265–273.
[31] Y.Y. Wu, S.Q. Zhou, F.H. Qin, X.Y. Ye, K. Zheng, Journal of Hazardous Materials 180 (2010) 456–465.
[32] T. Olmez-Hanci, I. Arslan-Alaton, G. Basar, Journal of Hazardous Materials 185 (2011) 193–203.
[33] I. Arslan-Alaton, N. Ayten, T. Olmez-Hanci, Applied Catalysis B: Environmental 96 (2010) 208–217.
[34] M. Sleiman, D. Vildozo, C. Ferronato, J.M. Chovelon, Applied Catalysis B: Environmental 77 (2007) 1–11.
[35] J. Chen, G. Li, Y. Huang, H. Zhang, H. Zhao, T. An, Applied Catalysis B: Environmental 123–124 (2012) 69–77.
[36] L.C. Chen, C.M. Huang, M.C. Hsiao, F.R. Tsai, Chemical Engineering Journal 165 (2010) 482–489.
[37] D.E. Gu, Y. Lu, B.C. Yang, Y.D. Hu, Chemical Communications (2008) 2453–2455.
[38] J. Yang, H.Z. Bai, Q. Jiang, H.S. Lian, Thin Solid Films 516 (2008) 1736–1742.
[39] P.W. Chou, S. Treschev, P.H. Chung, C.L. Cheng, Y.H. Tseng, Y.J. Chen, M.S. Wong, Applied Physics Letters 89 (2006).
[40] A.P. Grosvenor, B.A. Kobe, M.C. Biesinger, N.S. McIntyre, Surface and Interface Analysis 36 (2004) 1564–1574.
[41] N.R. Mathews, M.A.C. Jacome, E.R. Morales, J.A.T. Antonio, Physica Status Solidi C 6 (2009) S219–S223.
[42] A. Patra, C.S. Friend, R. Kapoor, P.N. Prasad, Chemistry of Materials 15 (2003) 3650–3655.
[43] N.C. Saha, H.G. Tompkins, Journal of Applied Physics 72 (1992) 3072–3079.
[44] D.P. Subagio, M. Srinivasan, M. Lim, T.T. Lim, Applied Catalysis B: Environmental 95 (2011) 414–422.
[45] P. Górska, A. Zaleska, E. Kowalska, T. Klimczuk, J.W. Sobczak, E. Skwarek, W. Janusz, J. Hupka, Applied Catalysis B: Environmental 84 (2008) 440–447.
[46] J. Fang, X.Z. Bi, D.J. Si, Z.Q. Jiang, W.X. Huang, Applied Surface Science 253 (2007) 8952–8961.
[47] K. Nagaveni, M.S. Hegde, G. Madras, Journal of Physical Chemistry B 108 (2004) 20204–20212.
[48] Y. Cong, J.L. Zhang, F. Chen, M. Anpo, Journal of Physical Chemistry C 111 (2007) 6976–6982.
[49] J.G. Yu, Q.J. Xiang, M.H. Zhou, Applied Catalysis B: Environmental 90 (2009) 595–602.
[50] D.K. Chatterjee, M.K. Gnanasammandhan, Y. Zhang, Small 6 (2010) 2781–2795.
[51] R.H. Myers, D.C. Montgomery, Response Surface Methodology: Process and Product Optimization Using Designed Experiments, Wiley, New York, 1995.
[52] S. Hwang, Y. Lee, K.Y. Yang, Biotechnology and Bioengineering 75 (2001) 521–529.
[53] D. Celik, E. Bayraktar, D. Mehmetoglu, Biochemical Engineering Journal 17 (2004) 5–13.
[54] E. Piera, M.I. Tejedor-Tejedor, M.E. Zorn, M.A. Anderson, Applied Catalysis B: Environmental 46 (2003) 671–685.
[55] A. Belyaeva, K. Baranova, Bulletin of Russian Academy of Science and Physics 73 (2009) 1056–1060.
[56] A.L. Linsebigler, G.Q. Lu, J.T. Yates, Chemical Reviews 95 (1995) 735–758.
[57] J.F. Suyver, R. Meester, J.J. Kelly, A. Meijerink, Physical Review B 64 (2001).
[58] A.G. Rincon, C. Pulgarin, Applied Catalysis B: Environmental 51 (2004) 283–302.
[59] W.Y. Choi, A. Termin, M.R. Hoffmann, Journal of Physical Chemistry 98 (1994) 13669–13679.